Gas-Phase Reactions of OH Radicals with Dimethyl Sulfoxide and Methane Sulfinic Acid Using Turbulent Flow Reactor and Chemical Ionization Mass Spectrometry

Alexander Kukui,* Dmitri Borissenko,† Gérard Laverdet, and Georges Le Bras

Laboratoire de Combustion et Systèmes Réactifs, CNRS, 1c av. de la Recherche Scientifique, 45071 Orléans Cedex 2, France

Received: December 11, 2002; In Final Form: May 13, 2003

Reactions of OH radicals with dimethyl sulfoxide $(CH_3)_2SO$ (DMSO) (reaction 1) and methane sulfinic acid $CH_3S(O)OH$ (MSIA) (reaction 2) have been studied at 298 K and 200 and 400 Torr of N_2 using a newly constructed high-pressure turbulent flow reactor coupled to an ion molecule reaction mass spectrometer. The experimental setup is discussed in detail. The reactions of OH with DMSO and MSIA were found to proceed with predominant formation of MSIA and SO_2, respectively. The yields of MSIA in reaction 1 and of SO_2 in reaction 2 were estimated to be 0.9 ± 0.2. The reaction rate constants $k_1 = (9 \pm 2) \times 10^{-11}$ cm^3 molecule^{-1} s^{-1} and $k_2 = (9 \pm 3) \times 10^{-11}$ cm^3 molecule^{-1} s^{-1} were obtained. These results indicate that the OH-addition route of the gas-phase atmospheric oxidation of dimethyl sulfide, CH_3SCH_3 (DMS), which produces DMSO as a primary intermediate, would result in high yields of SO_2, which is a precursor of H_2SO_4. The results then suggest that the other major end product of DMS oxidation, methane sulfonic acid CH_3SO_3H (MSA), would not be produced by gas-phase reactions involving MSIA as suggested so far, but rather by liquid-phase reactions.

1. Introduction

The need for accurate chemical kinetic and mechanistic data under atmospheric conditions is widely anticipated. This is especially true for radical-molecule reactions proceeding via short-lived complexes. Extrapolation of the data obtained for such reactions at low pressure (a few Torr) and room temperature are often problematic, because of possible non-Arrhenius rate constants behavior and different reaction mechanisms at different pressures and temperatures. The fast-flow technique has been widely used for gas kinetic studies. However, until recently, because of requirements imposed by the plug flow approximation[1,2] this technique was limited to low pressures, less than a few Torr, and often suffered from interaction of radicals with the reactor walls, especially at low temperatures. Seeley et al.[3] have developed a high-pressure turbulent flow technique in which effective plug flow conditions are established by fast turbulent mixing of reagents at the molecular level and by rapid radial turbulent diffusion to produce quasi-constant radial concentration profiles. Several variants of this technique has been used for kinetic studies at high pressure (50−760 Torr) by several groups using chemical ionization mass spectrometry[4,5] or optical[6,7] methods for the detection of the neutral species. Recently this technique has been also employed for studies of ion molecule reactions at high pressure.[8,9]

In this report, we present a new experimental setup for gas-phase kinetic studies in which a high-pressure turbulent flow reactor is combined with ion molecule reactor mass spectrometry detection. We also present kinetic and mechanistic results obtained with this technique for the OH reactions with dimethyl sulfoxide, $(CH_3)_2SO$ (DMSO), and methane sulfinic acid, $CH_3S(O)OH$ (MSIA):

$$OH + (CH_3)_2SO \rightarrow \text{products} \quad (1)$$

$$OH + CH_3S(O)OH \rightarrow \text{products} \quad (2)$$

DMSO is considered to be an important reaction intermediate in the atmospheric oxidation mechanism of dimethyl sulfide (DMS). The DMS oxidation has been suggested to play a significant role in the formation of clouds by producing new sulfate particles that act as cloud condensation nuclei (CCN).[10] Recent field measurements in the marine boundary layer,[11,12] as well as laboratory chamber studies,[13−17] indicate high DMSO yield from the DMS oxidation. DMSO in the atmosphere is considered to be formed mainly through the O_2-dependent addition channel of the reaction of DMS with OH[16−18] and, to some extent, through the reaction of DMS with BrO radicals.[19−22] Regarding the fate of DMSO in the atmosphere, both heterogeneous conversion by uptake on aerosol and cloud droplets[23] and gas phase reactions, mainly with OH, are considered to be important.

In previous studies[15,24−27] the reaction of DMSO with OH has been found to be very fast with a rate constant of $(6-10) \times 10^{-11}$ cm^3 molecule^{-1} s^{-1} at room temperature. Available results concerning the mechanism of this reaction are more controversial.[15,25,26] In a recent study of Urbanski et al.[26] the mechanism with predominant MSIA formation was suggested from the observation of CH_3 by IR absorption spectroscopy with a unity yield at 20 Torr pressure:

$$OH + (CH_3)_2SO \rightarrow CH_3S(O)OH + CH_3 \quad (1a)$$

This mechanism is also supported by a very recent reaction chamber study[28] where MSIA was observed as the major product of the OH-initiated oxidation of DMSO in air. A recent ab initio study[29] also supports formation of MSIA by reaction 1a. However, these recent findings of high yields of MSIA in the OH + DMSO reaction need to be confirmed, especially at atmospheric pressure.

* Present address of corresponding author: Service d'Aéronomie, CNRS. E-mail: kukuy@cnrs-orleans.fr.

† Present address: Institute for Energy Problems of Chemical Physics, Moscow, Russia.

10.1021/jp0276911 CCC: $25.00
Published on Web 07/08/2003

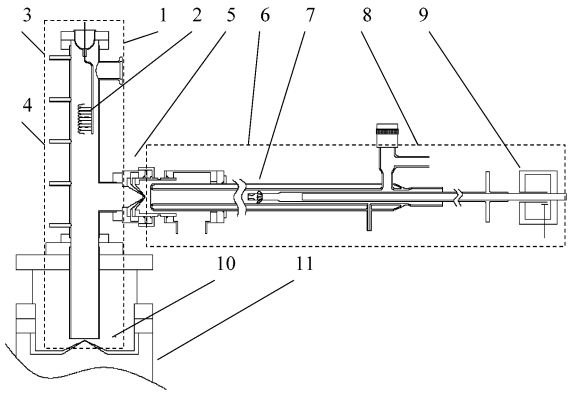

Figure 1. Experimental setup: 1, ion molecule reactor (IMR); 2, ion source; 3, carrier gas entrance port; 4, SF_6 entrance port; 5, HPTFR−IMR interface; 6, high-pressure turbulent flow reactor (HPTFR); 7, "Turbulizer"; 8, N_2 main flow entrance; 9, microwave discharge; 10, ion sampling; 11, mass spectrometer.

The high yield of MSIA in reaction 1 implies a significant role of MSIA in the mechanism of atmospheric DMS oxidation. Most probably, the fate of MSIA in the atmosphere will be a combination of gas phase and heterogeneous reactions. The reaction of MSIA with OH, which is expected to be predominant in the gas phase, may lead to either SO_2 or methane sulfonic acid (MSA) formation.

In this study we present evidence for MSIA formation in reaction 1 and for high SO_2 yield in the reaction 2 at 200 and 400 Torr of N_2.

2. Experimental Section

The instrumental setup is presented schematically in Figure 1. It consists of three main components: the high-pressure turbulent flow reactor (HPTFR), the ion molecule reactor (IMR), and the mass spectrometer. Reactions are studied in the fast-flow HPTFR operating either at high pressures between 50 and 700 Torr or at low pressure of about 2 Torr. A small fraction of the gas flow from the HPTFR is sampled via an interface into the IMR. In the IMR the species are selectively converted into secondary ions via ion molecule reactions with the primary ions produced in an ion source. The secondary ions are sampled via an interface and detected by mass spectrometry.

In the following sections of this section a detailed description of the main components is given. Also, some important aspects of kinetic measurements in the turbulent flow tube and the determination of effective flow velocities are discussed.

2.1. Experimental Setup. *Ion Molecule Reactor*. The IMR is made of a 4 cm i.d. 40 cm long stainless steel tube. The flow of carrier gas, about 3 l min^{-1} (STP) of He or Ar passed via a molecular sieve trap at liquid nitrogen temperature, is introduced via the entrance at the upstream end of the IMR and pumped with a 490 m^3 h^{-1} roots pump (WKP 500 A, Pfeiffer) in combination with a Pfeiffer DUO 065 rotary vane pump. The pressure in the IMR can be varied from 0.5 to about 10 Torr and was usually about 1 Torr.

Ions are sampled from the IMR via a 0.3 mm diameter aperture in a nickel cone maintained at a potential of about 20 V with opposite polarities for detection of positive and negative ions. In the first pumping stage of the vacuum interface between the IMR and the mass spectrometer ($P \approx 10^{-5}$ Torr, 500 L s^{-1} turbomolecular pump EXT501, Edwards), the ions are collected and focused on a second stage aperture with a set of electrostatic lenses (Extrel). In the second pumping stage ($P \approx 10^{-7}$ Torr, 300 L s^{-1} turbomolecular pump TPU 330, Balzers), the ions are further focused and directed with an electrostatic quadrupole deflector into an Extrel 3/4' quadrupole analyzer ($m/z_{max} = 500$). The ion current is measured in ion-counting mode with a Channeltron multiplier and MTS-100 preamplifier V7 (ARI Corp.). Data acquisition and ion optics potentials/mass analyzer control were performed with a Merlin Automation Data System (Extrel).

Primary positive ions and free electrons are produced in an ion source placed several centimeters downstream from the carrier gas entrance. The ion source consists of a heated thoriated iridium filament cathode surrounded by an anode made of tantalum spiral and biased to 0.1−0.2 V relative to ground potential. The electron energy is regulated by potential difference between these two electrodes and is varied depending on the ionization potential of the primary ion precursor. Usually the measured potential difference was 1−2 V above the corresponding ionization potential. In this work the primary positive ions were produced either by ionization of the carrier gas or by ionization of Xe traces added to the main flow.

Primary negative ions, SF_6^-, are produced by attachment of quasi-thermalized electrons to SF_6 added to the flow via an entrance localized 2 cm downstream from the ion source.

When Xe is used as the positive ion precursor with addition of SF_6, the main peaks in the positive spectrum are those from Xe^+ isotopes, while the negative spectrum is dominated by the signal at $m/z = 146$ from SF_6^-. The signal intensities of all Xe^+ isotopes or of SF_6^- were typically about $2-5 \times 10^7$ cps, estimated from the corresponding isotope peaks of lower intensity. The signal intensities of positive ions were about 10 times higher in the presence of SF_6, possibly due to the smaller coefficient of ambipolar diffusion, as well as because of reduced charge repulsion of the ions, both leading to slower loss of the ions at the reactor surface. The ion signal intensity at $m/z = 127$ corresponding to SF_5^- was 10^{-3} that of SF_6^-. Considering the dependence of SF_5^- and SF_6^- yields on the electron energy from the electron attachment to SF_6 at pressures close to that in our ion molecule reactor,[30] the ratio of SF_6^- and SF_5^- signals indicates that the electrons are thermalized before the point of SF_6 addition.

A portion of gas from the HPTR is sampled into the IMR via a 1 mm diameter aperture in a Teflon cone. The flow into the IMR is proportional to the pressure in the HPTFR varying from 1 L min^{-1} (STP) at 100 Torr to 5 L min^{-1} (STP) at 600 Torr of N_2 in the flow reactor. This results in concentrations of neutral reactant in the IMR of about 10^{-3} of that in the HPTFR.

The linear dynamic range of the instrument is determined by the low depletion of primary ions in ion molecule reactions, while the limit of detection depends on the corresponding ion molecule reaction rate constant and intensity of the background signals. The distance from the interface to the mass spectrometer sampling orifice is 21 cm, so the typical ion molecule reaction time is about 2−3 ms. The detection limits at this reaction time for the species detected using ion molecule reactions with rate constants $\approx 10^{-9}$ cm^3 $molecule^{-1}$ s^{-1} are about 10^8 molecule cm^{-3} in HPTFR (using the standard definition $S/N = 3$ and signal integration time of 20 s). The linear dynamic range ($R^2 > 0.995$) was measured to be 4−5 orders of magnitude. Example of NO_2 detection using reaction with SF_6^- is presented in Figure 2. The rate constant for the reaction of NO_2 with SF_6^- is 1.4×10^{-10} cm^3 $molecule^{-1}$ s^{-1} [31] and the detection limit derived from the calibration curve is 5×10^8 molecule cm^{-3}. As a rule, we found a correlation between the sensitivity and the corresponding ion molecule rate constants for different species. However, the ratio of the sensitivities was not always

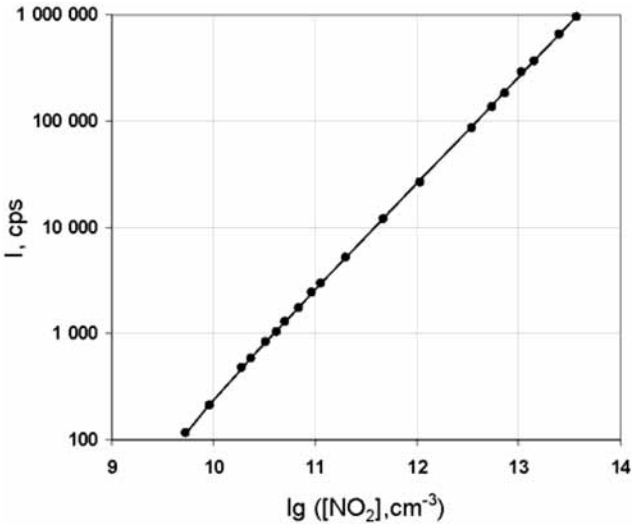

Figure 2. Dependence of NO_2^- signal on NO_2 concentration in the high-pressure flow reactor at $p = 214$ Torr. The solid line is a linear regression fit, $I(\text{cps}) = 2.6 \times 10^{-8} \times [NO_2]$.

equal to the known literature rate constant ratio. Observed differences were up to 30% and may be explained by a discrimination in the ions sampling and transport systems.

High-Pressure Turbulent Flow Reactor. The HPTFR consists of a main tube and two concentric injectors. The inner injector is a 6 mm i.d. 90 cm long quartz tube in which primary active species are produced by a microwave surface-wave discharge (SAIREM, 2.45 GHz, 300 W) operating at pressures from 1 to 700 Torr. Usually, He (2.5 L^{-1} min^{-1} STP) has been used as the carrier gas for the discharge source. The residence time in the injector is 30−160 ms, depending on the pressure. To reduce water impurities, the carrier gas was purified with molecular sieves at liquid nitrogen temperature.

The outer injector is a 11 mm i.d. tube terminating by a 6 mm i.d. × 8 mm o.d. injector with apertures around a spherical ending. The flow from the injector is directed perpendicularly to the main flow direction, speeding up the reactants mixing. The carrier gas in the outer injector was nitrogen. This mass flow rate was about 30% of the flow rate through the main flow tube. At this flow rate the flow in the outer injector is turbulent with a Reynolds number, *Re*, approximately equal to that in the main flow tube. The distance between the ends of both injectors can be adjusted by moving the inner injector. In the experiments of this work this distance was about 20 cm.

The main reactor is a 2.4 cm i.d. × 80 cm long glass tube. For high-pressure experiments, nitrogen from the liquid nitrogen tank is used as a carrier gas. The N_2 is purified with molecular sieves, which can be cooled to the temperature of liquid nitrogen. The reactor is evacuated with a 46 m^3 h^{-1} rotary pump (SOGEVAC SV40, Leybold). The flow rate (260 L min^{-1} STP maximum) is controlled with independently calibrated mass flow meters. Pressure is controlled with MKS capacitance manometers. The current setup allows the N_2 flows with maximum *Re* number of about 15 000. Taking a minimum *Re* number providing adequate conditions for kinetic studies to be 2300 (see below), the following limiting pressure-velocity conditions can be used at 300 K: $2 \div 11$ m s^{-1} at 700 Torr and $20 \div 150$ m s^{-1} at 50 Torr of N_2.

A fan-shaped turbulizer is placed about 2 cm upstream of the injector ending. Its position and shape have been optimized to achieve the fastest reactant mixing. The mixing of reactants at the macrolevel was verified by measuring the signal of a species, e.g. NO_2, added via the injector vs injector position.

TABLE 1: Effective Flow Velocity at Different Pressures and *Re* Numbers Obtained Using O_3 + NO as the Reference Reaction

P, Torr	[NO], 10^{16} molecule cm^{-3}	Re	V_0, m s^{-1}	v_{eff}/v_0
203.4	0.41−1.78	2606	6.42	1.19
201.0	0.06−1.72	2939	7.30	1.31
100.4	0.24−2.4	4820	23.92	1.26
201.6	0.31−1.54	4809	11.95	1.27
409.4	0.45−1.71	4883	5.94	1.21
205.4	0.54−2.9	6544	15.93	1.14
201.8	0.51−0.93	8098	20.05	1.21
201.2	0.42−1.94	9712	24.09	1.15
201.7	0.43−1.93	9785	24.16	1.31
407.7	0.88−1.87	9928	12.05	1.27
				$1.23 \pm 0.12(2\sigma)$

At the optimum position of the turbulizer the signal depends on the injector position only at distances less than 3 cm for *Re* numbers from 2300 to 12 000. This dependence was found to be sensitive to the ratio of mass flow rates through the injector, Q_{inj}, and the main reactor, Q_{main}. The weakest dependence corresponded to the flow rates ratio $Q_{inj}/Q_{main} = 0.3$ at which the *Re* numbers of the flows in the injector and in the main flow are approximately equal.

Mixing and Effective Velocity in the Turbulent Flow. In the turbulent pipe flow the concentration distribution is influenced by turbulent mixing, which is a complex combination of mixing processes on different scales, i.e., macromixing on a scale compared with the tube radius, inertial-convective and viscous-convective mesomixing on scales small compared to the tube radius, and finally viscous-diffusive micromixing on the scale where molecular diffusion becomes important.[32] For gases, Schmidt number $Sc \approx 1$, the macromixing and mesomixing steps are the limiting steps determining an effective rate of turbulent diffusion processes. One of the main conclusions made by Seeley et al.[3] and confirmed later by others is that for typical reaction rates of 50−300 s^{-1} the effective turbulent diffusion coefficients at $Re = 2000-10000$ are high enough to ensure plug flow conditions by fast radial mixing at pressure 50−760 Torr. According to the estimation of Seeley et al.,[3] the turbulent diffusion coefficients are about 250 cm^2 s^{-1} and independent of the *Re* number. For typical reaction rates and flow velocities in fast-flow experiments, the correction for the axial diffusion also will be small. It has also been shown by Seeley et al.[3] that fast initial mixing of reactants on the distance of several centimeters may be realized using a fan-shaped "turbulizer".

The effective flow velocity is another important issue that should be addressed for the treatment of kinetic data in the turbulent reactor (Table 1). The turbulent pipe flow is well divided into the viscous sublayer immediately adjacent to the wall where turbulence is negligible and a turbulent core separated by a buffer zone where both eddy and molecular viscous stresses are important.[33] Because of the slow mass exchange between the turbulent core and the layer close to the wall, the radial mixing is limited to the core region. As a result, the effective flow velocity relevant to the measured concentration gradients is determined by the average velocity of the turbulent core. According to the existing empirical relations, the radial velocity distribution in the turbulent core is more flat than in the laminar flow and depends on the *Re* number.[33] These relations, however, are accurate only for the fully developed turbulence in limited range of *Re* numbers and for the well-defined pipe roughness. The conditions are usually not met in the turbulent fast flow experiments. As well, the end effect of an injector and of a sampling cone may influence the velocity

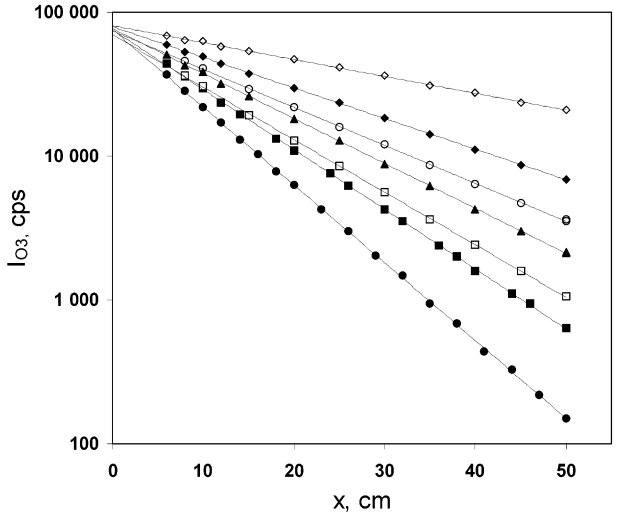

Figure 3. Dependence of O_3 signal on the injector position at P = 201.2 Torr, v_0 = 24.1 m s^{-1}, Re = 9712, $[O_3]_0 = 4.5 \times 10^{12}$ molecule cm^{-3}, $[NO]_0 = (4.24 \div 19.4) \times 10^{15}$ molecule cm^{-3}.

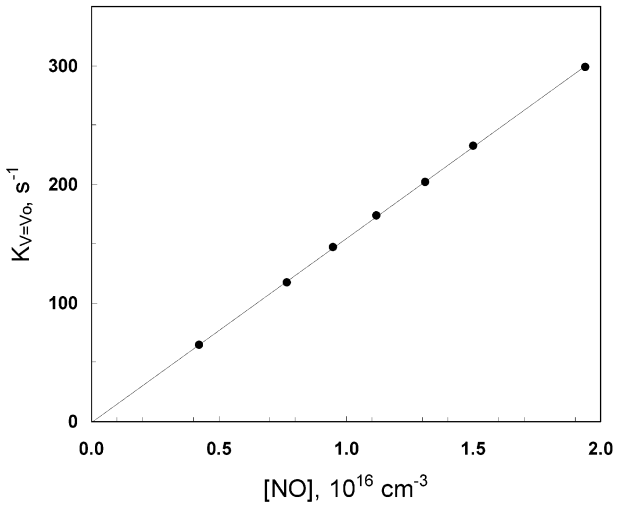

Figure 4. Dependence of the observed first-order rate constant on NO concentration for the reaction of O_3 with NO under experimental conditions of Figure 1 and assuming an effective flow velocity equal to the bulk velocity v_0. The slope of this linear dependence corresponds to the rate coefficient $(1.56 \pm 0.01) \times 10^{-14}$ cm^3 molecule^{-1} s^{-1}.

distribution. Hence, for particular experimental conditions the effective flow velocity should be empirically determined.

To verify the validity of plug flow approximation and for the measurement of effective flow velocity we have measured O_3 concentration decay in the well-studied reaction with NO:[34]

$$O_3 + NO \rightarrow O_2 + NO_2 \qquad (3)$$

NO has been added to the main reactor via the entrance located about 10 cm upstream from the injector end at the largest injector−sampling cone distance. Excess NO concentration was varied from 4.24×10^{15} to 1.94×10^{16} molecule cm^{-3}. NO has been cleaned from NO_2 and from higher oxides by passing it through a glass tube filled with solid iron(II) sulfate ($FeSO_4 \cdot 5H_2O$) and a trap cooled to 195 K (ethanol slush). Nevertheless, NO_2 traces have been observed at the m/e = 46 signal.

Ozone was produced from oxygen prior to the experiments with a commercial corona discharge ozone generator and stored in the 9 L vessel diluted with He (about 1% O_3/He). The initial ozone concentration was about 4×10^{12} molecule cm^{-3}.

Ozone was detected as O_3^- ion (m/z = 48) produced in the reaction of SF_6^- with O_3 ($k = 2.2 \times 10^{-10}$ cm^3 molecule^{-1} s^{-1}).[35] The contribution from NO_2 present as an impurity in NO and formed in the reaction of O_3 with NO has been accounted for by measuring the signal of NO_2 at m/z = 46 corresponding to the NO_2^- formed in the reaction of SF_6^- with NO_2 ($k = 1.4 \times 10^{-10}$ cm^3 molecule^{-1} s^{-1}).[31] The contribution of NO_2 to the m/z = 48 was independently measured and has been found to correspond to the abundance of the ^{18}O isotope, $I_{48}(NO_2) = 0.004 I_{46}(NO_2)$.

The dependences of ozone concentration on the position of the injector have been measured. These dependences were exponential (See Figure 3) in the range of Re numbers 2500−10 000 for the injector−sampling cone distances in the range 5−55 cm. Dependences of the observed first-order rate constants on the NO concentrations were also linear (Figure 4). Using the expression of the diffusional corrections for the parabolic velocity distribution,[2] we estimated that for statistically adequate description of these dependences the turbulent diffusion coefficient should be higher than 500 cm^2 s^{-1}, independent of the pressure and turbulence intensity. Because of the radial velocity profile flatness in the turbulent core, the use of the parabolic distribution may lead to an overestimation of the diffusion coefficient. Accounting for this effect, the above estimation is in agreement with the results of Seeley et al.[3]

Bimolecular rate coefficients calculated from the slopes of these dependences using the bulk flow velocities to find the reaction times were about 20% lower than the value $k_3 = (1.8 \pm 0.2) \times 10^{-14}$ cm^3 molecule^{-1} s^{-1} recommended by JPL at room temperature.[34] Assuming that this difference was due to the difference between the effective core velocity v_{eff} and the bulk flow velocity v_0, the dependence of the ozone signal intensity on the injector−sampling distance x and NO concentration, $I_{O_3}(x,[NO])$, may be expressed as $I_{O_3}(x,[NO]) = I_{O_3}^0 \exp\{-k_3[NO]t_{eff}(x)\}$, where $I_{O_3}^0$ is the intensity in absence of NO, k_3 is the JPL recommended value for the O_3+NO reaction rate constant, x is the injector−sampling distance, and $t_{eff}(x) = \{x\}/\{v_{eff}(x)\}$ is the effective reaction time. Using this expression for $I_{O_3}(x,[NO])$, the effective reaction time $t_{eff}(x)$ may be expressed as $teff(x) = -\partial \ln I_{O_3}(x,[NO])/\partial[NO] \times 1/k_3$. The values of $\partial \ln I_{O_3}(x,[NO])/\partial[NO]$ for different distances x were derived from the slopes of the plots $\ln\{I_{O_3}(x,[NO])\}$ vs concentration, which were found to be linear. The corresponding experimental dependences $t_{eff}(x)$ vs x were obtained by plotting the experimentally determined values of $t_{eff}(x) = \partial \ln I_{O_3}(x,[NO])/\partial[NO] \times 1/k_3$ vs x. These dependences, shown in Figure 5, were found to be linear, indicating that the effective velocity v_{eff} was independent of the injector position in the range x = 5−50 cm. Within the accuracy of the measurements, the ratios of v_{eff} determined from slopes of these dependences to the bulk flow velocities v_0, v_{eff}/v_0, were independent of pressure for P = 100−400 Torr and Re = 2600−10 000 with the mean value $v_{eff}/v_0 = (1.23 \pm 0.12)$. In other studies[3,6,8] this ratio was measured directly and found to decrease from about 1.2 at Re = 2000 to 1.05 at Re = 10 000, in accordance with theoretical prediction.[33] The v_{eff}/v_0 value measured in this study is in fact an experimental parameter, which may reflect not only the flow velocity far from the injector and sampling but also other reacting flow parameters related to mixing and flow pattern near the flow disturbing regions. This may be the reason for the independence of v_{eff}/v_0 on the Re number found in this work. On the other hand, within the accuracy limits of present measurements the value $v_{eff}/v_0 = (1.23 \pm 0.12)$ is consistent with measurements in other studies. Also, the value of v_{eff}/v_0 found in this work is in good agreement with the correction derived in another previous study for Re =

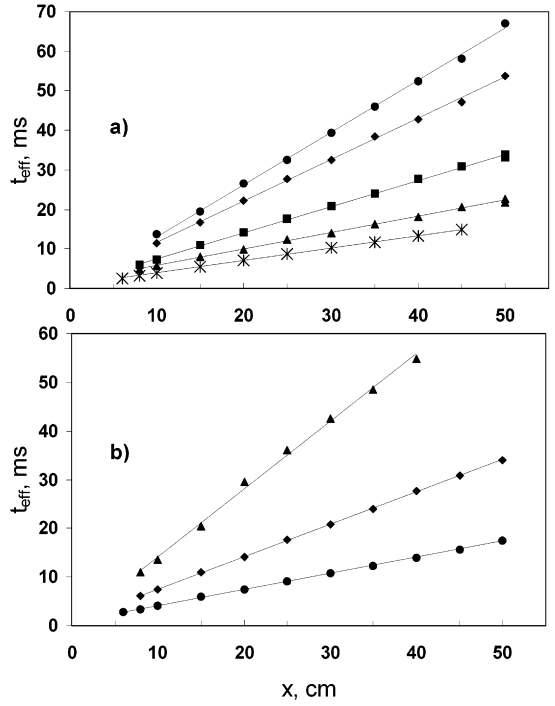

Figure 5. Plots of effective reaction time vs injector position determined from the temporal profiles of O_3 concentrations in reaction with NO using reaction rate constant $k_3 = 1.8 \times 10^{-14}$ cm^3 molecule^{-1} s^{-1}. (a) Dependences at a pressure of about 200 Torr for different *Re* numbers: *Re* = 2606, 2939, 4808, 8098, 9785. (b) Dependences at Re ≈ 4850 for different pressures: *P* = 100.4, 201.6, 409.4 Torr.

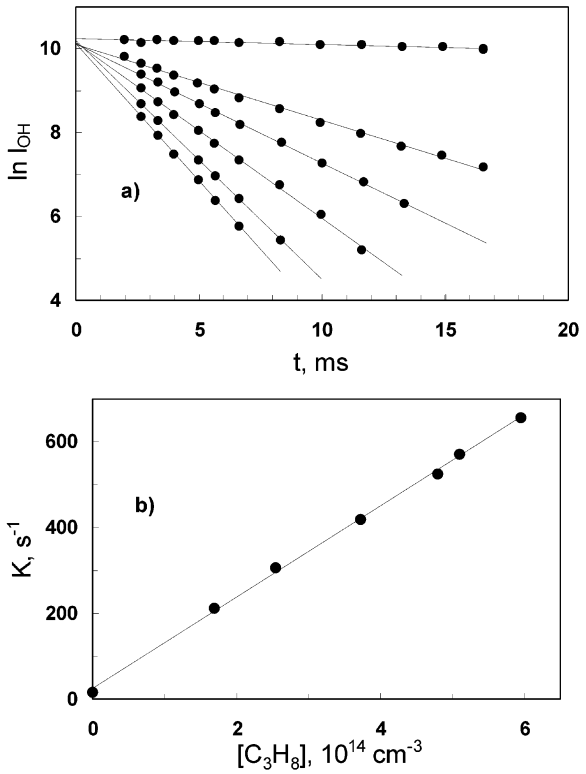

Figure 6. Kinetics data for the reaction of OH with C_3H_8 at *P* = 200.1 Torr, *Re* = 9867, $v_0 = 24.5$ m s^{-1}. (a) Plots of the OH signal vs reaction time calculated using $v_{eff}/v_0 = 1.23$ at different propane concentrations; (b) Plot of the first-order rate constant vs propane concentration.

4500−6000 using the reference reaction OH + *n*-butane.[7] We used the coefficient 1.23 to correct the velocities v_0 calculated from the measured volumetric flow rates and reactor pressure and added related uncertainty of 10% to the estimated systematic errors of kinetic measurements. We estimate that the total possible systematic error limiting the accuracy of the kinetic measurements is ±20%.

One of the test reactions studied with the present setup was reaction of OH with C_3H_8. The OH radicals were produced in the injector using reaction of F atoms with H_2O. F atoms were produced by dissociation of F_2 in the Surfatron microwave discharge. The results of these measurements at 200.1 Torr and *Re* = 9867 are presented in Figure 6, from which the bimolecular reaction rate constant $k = (1.06 \pm 0.04) \times 10^{-12}$ cm^3 molecule^{-1} s^{-1} at $T = 298$ K was found as the slope of the straight line in Figure 6b. The given uncertainty is the statistical error (2σ). The systematic error related to the effective flow velocity measurements was not included. Also, no diffusional correction was applied, which would have increased the rate constant by about 5%, assuming a parabolic velocity distribution and using the turbulent diffusion coefficient of 50 cm^2 s^{-1}, the lower value estimated by Seeley et al.[3] The obtained value is in good agreement with the JPL recommendation $k = (1.1 \pm 0.2) \times 10^{-12}$ cm^3 molecule^{-1} s^{-1}. The intercept 22 ± 17 s^{-1} in Figure 6b is somewhat larger than usually observed in our experiments for the first-order OH radicals loss rates of 10−20 s^{-1} in absence of other reactants.

The applicability of the turbulent flow technique presented in this work for the studies of higher order kinetics has been verified by simulation of the observed temporal profiles of reactants and products in the reaction systems with approximately equal initial reactant concentrations, including several consecutive steps. For example, temporal profiles of NO_2, OH, O, NO_3, and HNO_3 in the reaction system H+NO_2 were monitored for the initial concentrations of H and NO_2 in the range $10^{11}-10^{13}$ molecule cm^{-3}. The temporal profiles monitored in these experiments were found to be in good agreement with simulated dependences, indicating that under our typical experimental conditions the plug-flow approximation may be used also for treatment of higher order kinetics.

2.2. Experimental Conditions for the Study of the OH + DMSO and OH + MSIA Reactions. Reactions OH + DMSO (1) and OH + MSIA (2) were studied at 298 K by monitoring temporal profiles of primary reactants, OH(OD) and DMSO, and reaction products at different $[DMSO]_0/[OH]_0$ and $[DMSO]_0/[OD]_0$ initial concentration ratios. Experiments were performed in the pressure range 200−400 Torr of N_2 and at flow velocities corresponding to Reynolds numbers from 5000 to 10 000.

The reaction of OH(OD) with DMSO was studied in excess of DMSO: [DMSO] = $(0.5-2.5) \times 10^{12}$ molecule cm^{-3} and [OH]([OD]) ≈ 5×10^{10} molecule cm^{-3}. MSIA has been identified as the major product of the OH(OD) + DMSO reaction (see below) and its reaction with OH(OD) was studied in an excess of OH(OD) over DMSO: $[OH]_0([OD]_0) = (1-3) \times 10^{12}$ molecule cm^{-3} and $[OH]_0/[DMSO]_0 = 3 \div 100$.

OH(OD) radicals were produced in the injector by the reaction of H(D) atoms with NO_2:

$$H(D) + NO_2 \rightarrow OH(OD) + NO \qquad (4)$$

Compared to other conventional methods used for the OH generation (e.g. F + H_2O reaction) this source of OH provides relatively simple means for OH calibration (see below). In addition, this source has been found to be cleaner, with less impurities being generated in the discharge. The NO_2 concentration was kept low, to minimize the influence of the reaction of OH with NO_2 in the main reactor compared to the reaction of

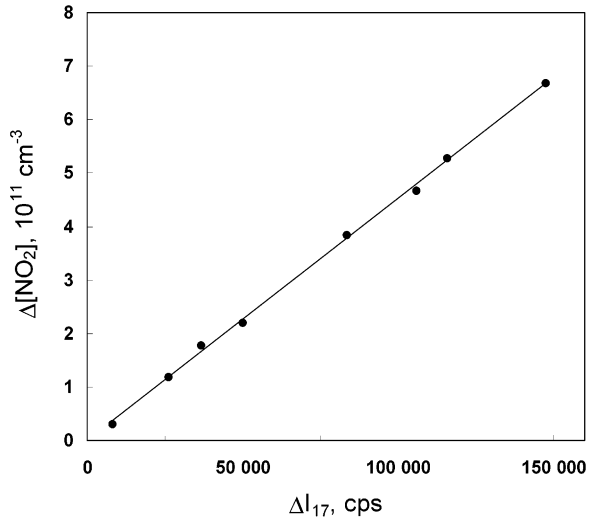

Figure 7. Example of OH calibration: dependence of NO_2 consumption vs OH signal obtained by varying the initial concentration of H atoms at constant initial concentration of NO_2: $P = 204$ Torr, $Re = 9908$, $v_{eff} = 29.8$ m s^{-1}, $t = 5$ ms, $[H]_0 \approx (0.05-2) \times 10^{12}$ molecule cm^{-3}, $[NO_2]_0 = 1.12 \times 10^{12}$ molecule cm^{-3}.

OH with DMSO and MSIA, but high enough to have a complete reaction of H with NO_2 in the injector. The reaction time in the injector was about 10 ms and the flow in the injector was turbulent. The H atoms were effectively consumed in the injector, resulting in a residual H atom concentration lower than 10^{10} molecule cm^{-3} at the entrance of the main reactor. According to kinetic simulation, the main coproducts of the OH source were NO, H_2O_2, HNO_3, and HONO. The concentration of O atoms was estimated to be less than 3×10^{10} molecule cm^{-3} for the highest OH concentrations, and this estimation was in agreement with the oxygen atom signal intensities at $m/z = 16$. Kinetics of the OH radicals, NO_2, and HNO_3 monitored in absence of DMSO were found to be in good agreement with the simulated ones, using literature reaction rate constants.

The OH and OD radicals were detected as OH^- and OD^- ions produced in the charge-transfer reaction with SF_6^-:[36]

$$SF_6^- + OH(OD) \rightarrow SF_6 + OH^-(OD^-) \qquad (5)$$

For calibration of the OH signal, H atoms produced in the injector were introduced into the main reactor flow containing NO_2. The dependences of the signal intensities at $m/z = 17$ (18), I_{17} (I_{18}), on the NO_2 consumption, ΔI_{46}, monitored at $m/z = 46$ as NO_2^- were measured by varying the H atom concentration. At reaction time of 5 ms and initial concentrations of the H and NO_2 reactants lower than 2×10^{12} molecule cm^{-3} used in these experiments, the secondary reactions of the produced OH were negligible and the measured dependences of I_{17} (I_{18}) vs ΔI_{46} were linear. An example of an OH calibration plot is presented in Figure 7. The relative OH to NO_2 sensitivity was derived from the slope of these dependences and was converted to the absolute OH sensitivity using independent calibration of the NO_2 signal. The OH sensitivity was found to be 5 ($\pm$0.5) times higher than the sensitivity for NO_2. Using a rate constant of 1.4×10^{-10} cm^3 molecule^{-1} s^{-1} for the $SF_6^- + NO_2$ reaction,[31] the $OH + SF_6^-$ reaction rate constant can be estimated as $k_5 = 7 \times 10^{-10}$ cm^3 molecule^{-1} s^{-1}. This value is 3 times lower than the ADO theory estimation.[36]

The validity of the OH calibration was also verified by monitoring the kinetics of OH, NO_2, and HNO_3 in the absence of DMSO under conditions of comparable concentrations of NO_2 and OH when the OH, NO_2, and HNO_3 kinetic behavior is dependent on NO_2 and OH concentrations. In all the experiments the observed absolute concentration profiles of OH and NO_2, as well as the relative HNO_3 concentration profiles, could be accurately simulated using the literature rate coefficients ($\pm$15%). NO_2, HNO_3, and O atoms were measured as NO_2^-,[31] $NO_3 \cdot HF^-$,[31] and O^- produced by reactions with SF_6^-.

DMSO (99.9% pure, Aldrich) was transferred into a Pyrex flask, degassed, and used without further purification. The DMSO was introduced into the reactor with the flow of He, $\sim$500 cm^3 min^{-1} STP, to which was added a small He flow passed over liquid DMSO maintained at 18 °C. The concentration of DMSO in the larger He flow was monitored by UV absorption at 213.9 nm (zinc lamp, 214 nm band-pass filter) in a 1 m length absorption cell situated at the entrance to the reactor. The DMSO concentration in the reactor was calculated using the absorption cross section value of 5.3×10^{-18} cm^2 molecule^{-1} [25] and known flow rates and pressures in the absorption cell and in the reactor. Because of DMSO adsorption−desorption processes on the inlet line surfaces, the time needed for obtaining a steady concentration, in particular at low [DMSO], was long (tens of minutes). This slow drift of the DMSO concentration and the uncertainty of the DMSO absorption cross section value were the main sources of uncertainties in this work.

DMSO was detected as $(CH_3)_2SO^+$ ion at $m/z = 78$ by the reaction

$$Xe^+ + (CH_3)_2SO \rightarrow Xe + CH_3S(O)CH_3^+ \qquad (6)$$

The $m/z = 78$ peak was the most intense in the positive spectrum of DMSO, with the peak intensities at $m/z = 79$ and 80 corresponding to S, O, and C isotope abundances. Comparing sensitivity for DMSO with sensitivities for other species detected using ion molecule reactions with known rate constants, the reaction of Xe^+ with DMSO appears to be fast, with a rate constant of about 10^{-9} cm^3 molecule^{-1} s^{-1}. This result is consistent with the ionization potential of DMSO being about 3 eV lower than that of Xe: IE(DMSO) = 9.2 eV.[37]

SO_2, the major product of the OH + MSIA reaction, was detected as FSO_2^- ($m/z = 83$) and $F_2SO_2^-$ ($m/z = 102$) using reaction with SF_6^-:[31]

$$SF_6^- + SO_2 \rightarrow SF_5 + FSO_2^- \qquad (7a)$$

$$\rightarrow SF_4 + F_2SO_2^- \qquad (7b)$$

The signal intensity at $m/z = 102$ in the SO_2 negative ion spectra was about twice that at $m/z = 83$, in fair agreement with the branching ratio $k_{7b}/k_{7a} = 0.27$ reported by Huey et al.[31]

3. Experimental Results

Product analysis in the reaction system OH + DMSO + NO_2 was performed by monitoring negative and positive ion mass spectra at different reaction times and different OH and DMSO concentrations. Typical differential negative ions mass spectra (discharge on/off) are shown in Figure 8 under conditions of excess OH and OD concentrations. The OH and OD radicals give rise to the peaks at $m/z = 17$ and 18, while NO_2 is consumed in the reactions with OH and H atoms. Peaks at $m/z = 62$, 66, 82 in the OH system and $m/z = 62$, 67, 83 in the OD system are from NO_3, H(D)ONO, and H(D)NO_3 formation, respectively, predominantly in the source of the OH/OD radicals.

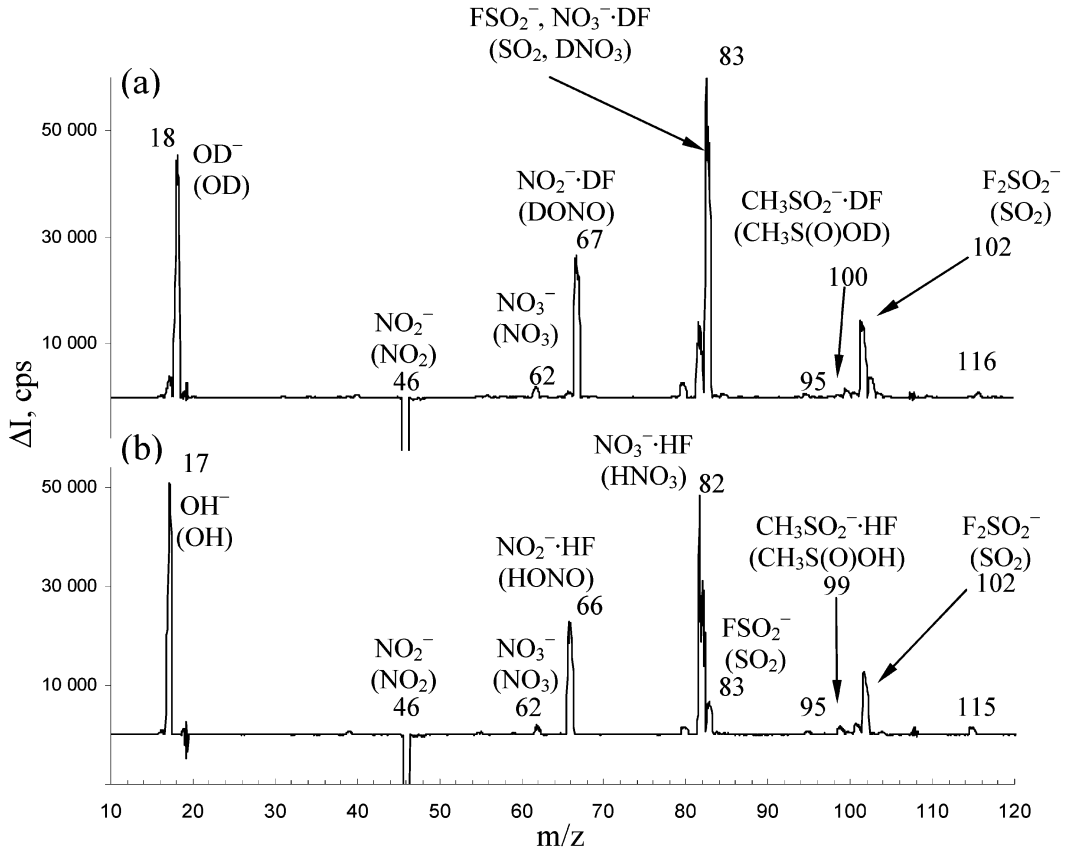

Figure 8. Typical differences of negative ions mass spectra with discharge on/off for the systems OD/NO_2/DMSO (a) and OH/NO_2/DMSO (b) in excess of OH/OD over DMSO. Experimental conditions: $P = 200$ Torr, $v_{eff} = 20.3$ m s^{-1}, $Re = 6633$, $t_{eff} = 16.3$ ms, $[OH]_0 \approx [OD]_0 \approx 1.5 \times 10^{12}$ molecule cm^{-3}, $[DMSO]_0 = 3.2 \times 10^{11}$ molecule cm^{-3}.

These peaks of approximately the same intensity are present also in the spectra obtained in absence of DMSO. In presence of DMSO, peaks appeared at $m/z = 102$ and 83 with the same intensity ratio as in the spectra of SO_2. In the OD + DMSO spectra the peak at $m/z = 83$ coincides with the $NO_3 \cdot DF^-$ signal. After subtraction of this contribution measured in absence of DMSO, the ratio I_{102}/I_{83} was found to be the same in both OH + DMSO and OD + DMSO reaction systems. With DMSO in excess the intensities of the $m/z = 102$, 83 peaks were very low, while at $[OH]_0 \geq [DMSO]_0$ the intensities of these peaks increased with reaction time, reaching quasi-stationary level at long reaction times, as shown in Figure 9.

Negative ion peaks at $m/z = 99$ (OH + DMSO) and $m/z = 100$ (OD + DMSO) appeared under both DMSO excess and [OH] ≥ [DMSO] experimental conditions. Under similar experimental conditions these peaks intensities were of similar magnitude and exhibited identical dependences on reaction time. In excess of DMSO they reached a stationary level with a formation rate equal to the rate of OH consumption (see Figure 9). Under conditions of $[OH]_0 \geq [DMSO]_0$, the signals reached a maximum and then decreased with reaction time, as shown in Figure 9. The same behavior was observed with positive ion signals at $m/z = 80$ (OH + DMSO) and $m/z = 81$ (OD + DMSO) (see Figure 9).

The above observations were explained by the mechanism including formation of MSIA by reaction of OH with DMSO (1a) followed by the reaction of MSIA with OH forming SO_2 (2a):

$$OH + CH_3S(O)OH \rightarrow CH_3 + SO_2 + H_2O \qquad (2a)$$

Formation of SO_2 was obvious from the increase of $m/z = 102$ ($F_2SO_2^-$) and $m/z = 83$ (FSO_2^-) signal intensities. The MSIA kinetics was monitored at $m/z = 99(100)$ for negative ions and at $m/z = 80(81)$ for positive ions. These signals were tentatively assumed to come from $CH_3SO_2^- \cdot HF$ at $m/z = 99$ ($CH_3SO_2^- \cdot DF$ at $m/z = 100$) and $CH_3S(O)OH^+$ at $m/z = 80$ ($CH_3S(O)OD^+$ at $m/z = 81$) according to the reactions 8 and 9:

$$SF_6^- + CH_3S(O)OH \rightarrow SF_5 + CH_3SO_2^- \cdot HF \qquad (8)$$

$$Xe^+ + CH_3S(O)OH \rightarrow Xe + CH_3S(O)OH^+ \qquad (9)$$

The assumed mechanism was supported by the appearance of the $m/z = 15$ signal in positive spectrum corresponding to the formation of CH_3 in both reactions 1a and 2a. However, as the reaction mechanism for the CH_3 conversion in the studied system was very complex, it was not analyzed.

Two other peaks, $m/z = 95$ and 115 (OH + DMSO) or $m/z = 116$ (OD + DMSO), were observed in the negative ion mass spectrum, when $[OH]_0 \geq [DMSO]_0$. They could correspond to the formation of MSA, which could result in formation of $CH_3SO_3^-$ and $CH_3SO_3^- \cdot HF/CH_3SO_3^- \cdot DF$ ions via reaction of MSA with SF_6^-. Yet, the intensities of these signals were about 100 times lower than the intensities of SO_2 signals (see discussion).

3.1. Experimental Results with Excess of DMSO. In these experiments DMSO concentrations were more than 10 times higher than that of OH radicals and the OH radicals were consumed predominantly in reactions with DMSO and NO_2. As shown in Figure 10, the OH decay plots were exponential and the slope of the first-order plot gives the bimolecular reaction rate coefficient $k_1 = (8.8 \pm 2.5) \times 10^{-11}$ cm^3 $molecule^{-1}$ s^{-1}. The uncertainty accounts for the accuracy of

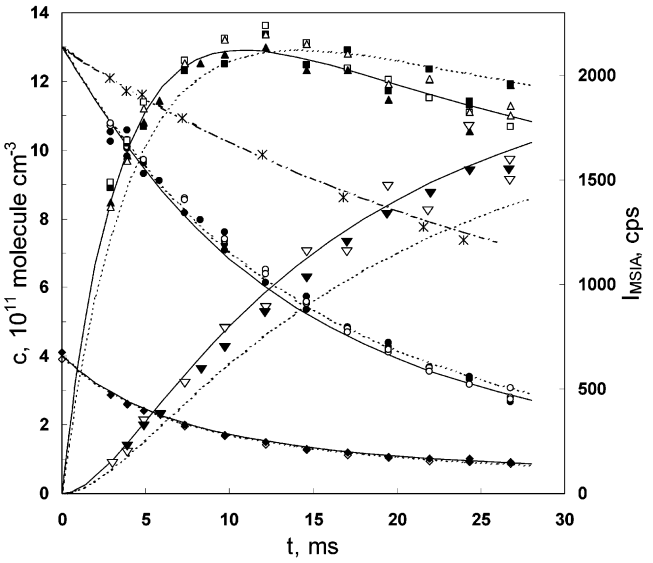

Figure 9. Temporal concentration profiles in the OH + DMSO (closed symbols) and OD + DMSO (open symbols) reaction systems in excess of OH (OD) over DMSO at $P = 203$ Torr, $v_{eff} = 20.5$ m s^{-1}, $Re = 6782$, $[OH]_0 = [OD]_0 = 1.3 \times 10^{12}$ molecule cm^{-3}, $[NO_2]_0 = 1.0 \times 10^{12}$ molecule cm^{-3}, $[DMSO]_0 = 4.0 \times 10^{11}$ molecule cm^{-3}. Presented are signal intensity profiles of $CH_3S(O)OH/CH_3S(O)OD$ (▲/△, $m/z = 99/100$; ■/□, $m/z = 80/81$; the signal intensities at $m/z = 99/100$ are scaled by 0.26 to fit the signal intensities on $m/z = 80/81$) and concentration profiles of DMSO(♦/◇, $m/z = 78$), OH/OD (●/○, $m/z = 17/18$), and SO_2 (▼/▽, $m/z = 102$). Concentration profile of OH in absence of DMSO is also presented (*). Solid and dashed lines correspond to the calculated dependences with $k_2 = 1.1 \times 10^{-10}$ and 7.6×10^{-11} cm^3 molecule^{-1} s^{-1}, respectively.

the DMSO concentration determination and the uncertainty associated with the effective flow velocity. The intercept of the first-order rate plot was about 40 s^{-1}, representing the contribution of the reaction OH + NO_2 to the loss rate of OH and an unknown first-order loss of about 10 s^{-1}.

Kinetics of the MSIA formation could be well-described with the reaction rate constant k_1 derived from the decay of the OH radicals as shown in Figure 10, where all solid lines corresponding to the increase of I_{99} signal intensities were calculated with the same value of $k_1 = 8.82 \times 10^{-11}$ cm^3 molecule^{-1} s^{-1}. The only adjustable parameter was the sensitivity coefficient for the MSIA detection, which was found to be the same within 10% for all DMSO concentrations. The dependence of the MSIA quasistationary signal level on the DMSO concentration is explained by the competition of the OH consumption by reactions with DMSO and with NO_2. The good description of the MSIA profiles using the rate constant derived from the OH decay rates is, in fact, an independent confirmation of the k_1 value relative to the OH + NO_2 reaction rate constant used to calculate the MSIA temporal dependencies (see Table 2).

Several experiments conducted at 200 and 400 Torr of N_2 under experimental conditions similar to that presented in Figure 10 reveled no pressure dependence of the reaction rate constant k_1. The mean value derived from these experiments is:

$$k_1 = (9 \pm 2) \times 10^{-11} \text{ cm}^3 \text{ molecule}^{-1} \text{ s}^{-1}$$

The scattering of the values derived from the different experiments was less than 5% (2σ), while the given uncertainty reflects the estimated uncertainties of flow velocity and DMSO concentration measurements.

3.2. Experimental Results with Excess of OH. Reaction of OH with MSIA was studied using an excess of OH over DMSO

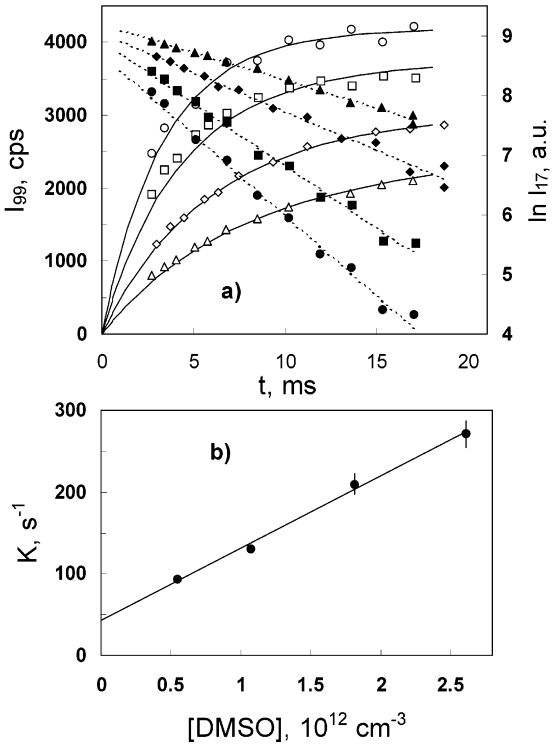

Figure 10. Kinetics of the OH + DMSO reaction in excess of DMSO. (a) OH exponential decays (solid symbols) and MSIA formation (open symbols) at $P = 200$ Torr, $v_{eff} = 29.4$ m s^{-1}, $Re = 9756$, $[OH]_0 = 6.5 \times 10^{10}$ molecule cm^{-3}, $[NO_2]_0 = 5.2 \times 10^{12}$ molecule cm^{-3}, $[DMSO]_0 = (0.54-2.61) \times 10^{12}$ molecule cm^{-3}. Dashed straight lines, linear regression fits; solid lines, dependences calculated using $k_1 = 8.82 \times 10^{-11}$ cm^3 molecule^{-1} s^{-1} obtained from the first-order plot presented in part b. (b) Plot of the first-order rate constant vs DMSO concentration.

at 200 and 400 Torr of N_2. The OH concentrations in different experiments were $(1-3) \times 10^{12}$ molecule cm^3, while the ratios of initial concentrations were $[OH]_0/[DMSO]_0 = 3 \div 100$. Typical temporal concentration profiles of DMSO, OH/OD, and SO_2, as well as temporal dependences of MSIA ion signal intensities at $m/z = 80$, 99 (OH) and 81, 100 (OD) are presented in Figure 9. The kinetics of MSIA exhibited a behavior typical of a primary product followed by consumption in secondary reactions. The SO_2 kinetics was typical of that of a secondary product without any indication of its consumption. As no other significant products could be identified from the observed mass spectra, we used for simulation the reaction mechanism presented in Table 2. In this mechanism, as a first approximation, the MSIA and SO_2 yields in the reactions of OH with DMSO and MSIA are taken to be unity. The reaction rate constant k_2 was derived by fitting individual experimental profiles to this reaction mechanism with k_2 being the only variable parameter. Simulation was performed using absolute concentrations profiles of DMSO, NO_2, OH, and SO_2. For the reaction of OH with DMSO the reaction rate constant derived in this work was used. Although included in the reaction scheme (Table 2), the reactions of O, H, and CH_3 radicals were of minor importance. Their influence on the k_2 rate constant and the value of SO_2 yield derived from the simulations was less than 10% for the conditions of these experiments. The scattering of the derived k_2 values was less than 20% (see Figure 9), with the mean value obtained from all experiments: $k_2(\pm 2\sigma) = (9 \pm 1.5) \times 10^{-11}$ cm^3 molecule^{-1} s^{-1}. Within this uncertainty range the value of k_2 was the same at pressure 200 and 400 Torr. Accounting for the estimated systematic errors results in $k_2 = (9 \pm 3) \times 10^{-11}$ cm^3 molecule^{-1} s^{-1}.

TABLE 2: Reactions Used for Simulation in the OH + DMSO Reaction System

reaction	k,[a] cm^3 molecule^{-1} s^{-1}	ref
$DMSO + OH \rightarrow CH_3 + CH_3S(O)OH$	9×10^{-11}	this work
$CH_3S(O)OH + OH \rightarrow CH_3 + SO_2 + H_2O$	9×10^{-11}	this work
$DMSO + O \rightarrow 2CH_3 + SO_2$	7.5×10^{-12}	46
$DMSO + CH_3 \rightarrow$ products	$<10^{-11}$	estimated
$CH_3 + OH \rightarrow CH_3OH$	7×10^{-11}	47
$CH_3 + NO_2 \rightarrow CH_3O + NO$	2.5×10^{-11}	48
$CH_3 + NO_2 \rightarrow CH_3NO2$	$(3.5\text{-}3.7) \times 10^{-11}$	49
$CH_3 + CH_3 \rightarrow C_2H_6$	6×10^{-11}	50
$CH_3O + NO_2 \rightarrow CH_3ONO_2$	1.4×10^{-11}	34
$H + NO_2 \rightarrow OH + NO$	1.3×10^{-10}	34
$H + OH \rightarrow H_2O$	$(4.45\text{-}8.9) \times 10^{-12}$	50
$OH + NO_2 \rightarrow HNO_3$	$(5.89\text{-}8.34) \times 10^{-12}$	51
$OH + OH \rightarrow H_2O_2$	$(2.57\text{-}4.11) \times 10^{-12}$	34
$OH + OH \rightarrow O + H_2O$	1.9×10^{-12}	34
$OH + O \rightarrow O_2 + H$	3.3×10^{-11}	34
$OH + H_2O_2 \rightarrow HO_2 + H_2O$	1.7×10^{-12}	34
$O + NO_2 \rightarrow O_2 + NO$	1×10^{-11}	52
$O + NO_2 \rightarrow NO_3$	$(1.55-2.75) \times 10^{-12}$	53

[a] $T = 298$ K; $P = 200-400$ Torr.

The assumed unity yields of MSIA and SO_2 in the reactions of OH with DMSO and MSIA, respectively, provided in fact the best fitting for the SO_2 concentration profiles, although a statistically adequate description of the SO_2 kinetics was also possible, assuming an approximately 20% lower yields of MSIA in reaction 1 or of SO_2 in reaction 2 (or a combination of these yields). These lower yields would, however, require lower reaction rate constants k_1 or k_2, which would not describe properly the experimental MSIA profiles. Hence, assuming that under conditions of our experiments DMSO and MSIA react only with OH radicals, the unity yields of MSIA and SO_2 in these reactions were needed for a good description of the concentration profiles. Finally, accounting for the accuracy of the OH and DMSO calibrations, we estimate the yields of MSIA in reaction 1 and of SO_2 in reaction 2 to be 0.9 ± 0.2.

4. Discussion

The rate constant for the reaction of OH with DMSO has been determined in this work from the OH decay kinetics in excess of DMSO and was consistent with the observed MSIA and SO_2 temporal profiles in the presence of an excess of DMSO and for $[OH]_0/[DMSO]_0 = 1 \div 100$. The value $k_1 = (9 \pm 2) \times 10^{-11}$ cm^3 molecule^{-1} s^{-1} found in this work at 298 K is in good agreement with two previous direct time-resolved measurements.[25,26] Hynes and Wine[25] used a pulsed laser photolysis/pulsed-laser-induced fluorescence technique and found $k_1 = (10 \pm 3) \times 10^{-11}$ cm^3 molecule^{-1} s^{-1} at room temperature and over the pressure range 25−700 Torr. Urbanski et al.[26] derived $k_1 = (8.7 \pm 1.6) \times 10^{-11}$ cm^3 molecule^{-1} s^{-1} at 20 Torr from the CH_3 formation rate using IR laser spectroscopy. The rate coefficients k_1 derived in two other studies conducted in reaction chambers using FT-IR spectroscopy are somewhat lower, although error range quotes in all studies are large: Barnes et al. [24] and Falbe-Hansen et al.[27] found $k_1 = (6.2 \pm 2.2) \times 10^{-11}$ and $(5.9 \pm 1.5) \times 10^{-11}$ cm^3 molecule^{-1} s^{-1}, respectively.

The kinetics on the ion masses corresponding to the $CH_3S(O)OH^+/CH_3S(O)OD^+$ and $CH_3SO_2^-\cdot HF/CH_3SO_2^-\cdot DF$ observed in this work and attributed to MSIA signals show evidence for the formation of $CH_3S(O)OH$ in the reaction of OH with DMSO. These measurements seem to be the first direct detection of MSIA in the gas phase, although independent verification of the ion peaks' identity was not performed. The yield of MSIA close to unity is in agreement with the mechanism proposed by Urbanski et al. [26] on the basis of the unity yield of CH_3 radicals measured in their work at 20 Torr total pressure. Reaction 1 has been proposed to proceed via an adduct formation, which may be followed by its decomposition to CH_3 + MSIA:

$$OH + (CH_3)_2SO + M \rightarrow (CH_3)_2S(O)\cdot OH + M \quad (10)$$

$$(CH_3)_2SO(O)\cdot OH + M \rightarrow CH_3S(O)OH + CH_3 + M \quad (11)$$

This mechanism has been recently supported by an ab initio study,[29] in which the CH_3 + MSIA product was found to be the dominant pathway of reaction 1. Also, a potential energy surface minimum has been localized, corresponding to the $(CH_3)_2S(O)\cdot OH$ addition complex with a binding energy of 50.7 kJ/mol.[29] The upper limit for the lifetime of the stabilized complex, if formed, has been estimated by Urbanski et al. [26] to be less than 10 μs at a pressure of 20 Torr.

In this study we found no indication of the stabilized complex formation. The yield of MSIA in the reaction of OH with DMSO was derived in this work indirectly from the absolute yield of SO_2. The SO_2 yield was found to be unity and independent of pressure in the range 200−400 Torr of N_2, indicating that effects related to complex formation were unimportant under our experimental conditions. The independence of MSIA yield on pressure follows also from the pressure independence of effective MSIA sensitivities derived from simulation using the reaction mechanism from Table 2.

Formation of a short-lived stabilized complex with a quasi-stationary concentration low relative to concentrations of MSIA and SO_2 cannot be excluded and it would be indistinguishable within the accuracy of our experiments. To be consistent with temporal profiles of this work, the maximum lifetime of such a stabilized adduct may be estimated as 10^{-4} s^{-1}.

We also analyzed the possibility of a complex formation followed by its reaction with OH. The likely product of such reaction would be $(CH_3)_2S(O)(O)$ ($DMSO_2$). In our experiments, however, no signals that could correspond to $DMSO_2$ were found.

In case of an adduct formation, its reaction with O_2 may be a source of $(CH_3)_2S(O)(O)$ in the atmosphere and in reaction chamber experiments:

$$(CH_3)_2S(O)\cdot OH + O_2 \rightarrow (CH_3)_2SO_2 + HO_2 \quad (12)$$

In several experiments that were performed in the presence of

oxygen at O_2 concentration of 3×10^{16} molecule cm^{-3}, we did not find any influence of O_2 on the temporal concentrations profiles of all the measured species. As well, negative and positive mass spectra obtained with and without O_2 were essentially identical, except for the appearance of some nonrelevant peaks related to O_2. Assuming an adduct formation, this result may be used to place a lower limit for the ratio of the adduct decomposition rate to the rate of its reaction with O_2, $(k_{decomp}/k_{12}[O_2]) > 1$. Assuming $k_{12} = 1 \times 10^{-12}$ moleculecm^{-3} s^{-1}, by analogy with the reaction of O_2 with the DMS−OH adduct, the upper limit for the $(CH_3)_2S(O)\cdot OH$ decomposition rate would be about 10^{-5} s^{-1}. This estimation gives the same upper limit as derived by Urbanski et al.[26] and may be too high, considering the low barrier to decomposition of about 6 kcal/mol obtained from ab anitio calculations.[29] Comparing this value with the stabilization energy of DMSO·OH addition complex of 13.3 kcal/mol,[38] one may expect that adduct stabilization and its reactions would be less important for the reaction OH + DMSO compared with OH + DMS.

The rate constant found in this work for the reaction of OH with MSIA, $k_2 = (9 \pm 3) \times 10^{-11}$ cm^3 molecule^{-1} s^{-1}, is about 10 times higher than that estimated by Yin et al.[39] Predominant formation of SO_2 in this reaction may be explained by considering a mechanism including formation of the chemically excited CH_3SO_2 radical followed by its "prompt" decomposition. We have proposed a similar mechanism for the reactions of CH_3SO with NO_2 and O_3:[40,41]

$$CH_3S(O)OH + OH \rightarrow CH_3SO_2^* + H_2O \qquad (2b)$$

$$CH_3SO_2^* \rightarrow CH_3SO_2 \qquad (13)$$

Reaction 2b may proceed either by direct abstraction of H atom or by OH addition to S followed by H_2O elimination and formation of CH_3SO_2. Excitation energy of the CH_3SO_2* radical may be estimated as about 60% of reaction exoergicity[42] for the direct abstraction mechanism and higher than 60% for the complex formation−elimination mechanism. The exoergicity of reaction 2b can be estimated to be about 38 kcal/mol, assuming a $CH_3S(O)O-H$ bond dissociation energy of 80 kcal/mol.[39] Hence, the excitation energy of about 23 kcal/mol will be available, which is high enough for fast decomposition considering a decomposition energy of 14.7 kcal/ mol.[40]

Formation of methylsulfonyl radical at very low concentrations could be, however, anticipated by considering the appearance of peaks at masses $m/z = 95$ and 115 (OH + DMSO) and 116 (OD + DMSO) (see the Experimental Section). These signals could be assigned to $CH_3S(O)(O)(OH)$ (MSA), the only conceivable pathway of its formation in the present reaction system being the addition reaction:

$$CH_3SO_2 + OH + N_2 \rightarrow CH_3S(O)(O)(OH) + N_2 \qquad (14)$$

Temporal dependences of the signals assigned to MSA could be described with the rate constants k_1 and k_2 of this work and using $k_{14} \geq 10^{-11}$ cm^3 molecule^{-1} s^{-1}. Considering maximum observed signal intensities corresponding to MSA and assuming MSA sensitivity to be similar to that of SO_2, the formation yield of MSA would be less than 5% of that of SO_2. The corresponding upper limit for the yield of stabilized CH_3SO_2 radical in reaction 2 may be also estimated as less than 5%. This estimation is consistent with the accuracy of SO_2 yield determination, which was about 20%.

5. Atmospheric Implications

In the atmosphere, both gas-phase and heterogeneous chemistry has to be considered to determine the fate of DMSO and MSIA.

In the gas phase, efficient conversion of DMSO to MSIA by reaction with OH is expected on the basis of the present results at high pressure and of Urbanski et al.[26] at 20 Torr. Formation of the stabilized addition complex $(CH_3)_2S(O)OH$ and its reaction with oxygen seem to be unimportant under atmospheric conditions. This conclusion is also supported by a recent smog chamber study,[28] in which high yields of MSIA from the OH-initiated DMSO oxidation in synthetic air have been observed.

In this work, the reaction of OH with MSIA has been found to be fast and, therefore, it should be considered as the main pathway of the gas-phase MSIA conversion under atmospheric conditions. Reaction of MSIA with ozone seems to be unimportant considering its rate constant of 2×10^{-18} cm^3 molecule^{-1} s^{-1} estimated by Yin et al.[39] Even at very high ozone concentration of 50 ppb, the rate constant of the reaction of MSIA with O_3 should be higher than 10^{-15} cm^3 molecule^{-1} s^{-1} to be competitive with the reaction with OH radicals. Considering also the high SO_2 yield in the reaction of MSIA with OH, about 100%, the main product of the gas-phase atmospheric DMSO oxidation seems to be the SO_2 with a characteristic time of DMSO to SO_2 conversion of about 5 h at a typical day time OH concentration of 3×10^6 molecule cm^{-3}.

The conclusion about the high efficiency of gas-phase DMSO to SO_2 conversion makes it possible to speculate about the significance of heterogeneous and liquid-phase processes in MSA formation from the atmospheric DMS oxidation. MSA is one of the major DMS oxidation products, and the likely mechanism of its formation in the gas phase was suggested to be the OH addition pathway of DMS oxidation leading to the MSIA formation, followed by conversion of the MSIA to MSA by reactions such as those with O_3 and O_2(+OH).[39,43,44] The model predictions, however, systematically underestimate the MSA production rate,[43,44] and discrepancies between field measurements and modeling results as large as 3−4 orders of magnitude[44] indicate that the mechanism of MSA formation is currently poorly understood. Attempts to improve the DMS oxidation model by modifying the gas-phase mechanism of MSA formation suggest a more efficient MSIA to MSA conversion.[43,44] According to the present work, however, the gas phase MSIA oxidation would result predominantly in SO_2 and consequently, H_2SO_4 formation. Another way to produce MSA would be its formation via reactions in the liquid phase. This mechanism seems to be more adequate in the light of our results. This conclusion about the significance of MSIA heterogeneous and liquid-phase chemistry with respect to the MSA formation mechanism is also in line with a recent study in aqueous medium,[45] where reactions of OH with DMSO and methanesulfonate (MSI^-) were found to be fast, with methanesulfonate (MS^-) identified as the major end product.

Acknowledgment. This work has been supported by the European Union through its environmental program (EL CID project). Financial support has also been provided by the Conseil Régional du Centre for equipment and fellowship of D.B. through the STUDIUM association.

References and Notes

(1) Howard, C. J. *J. Phys. Chem.* **1979**, *83*, 3.
(2) Kaufman, F. *J. Phys. Chem.* **1984**, *88*, 4909.

(3) Seeley, J. V.; Jayne, J. T.; Molina, M. J. *Int. J. Chem. Kinet.* **1993**, *25*, 571.
(4) Elrod, M. J.; Ranschaert, D. L.; Schneider, N. J. *Int. J. Chem. Kinet.* **2001**, *33*, 363.
(5) Lipson, J. B.; Elrod, M. J.; Molina, M. J. *J. Chem. Soc., Faraday Trans.* **1997**, *93*, 2665.
(6) Herndon, S. C.; Villalta, P. W.; Nelson, D. D.; Jayne, J. T.; Zahniser, M. S. *J. Phys. Chem. A* **2001**, *105*, 1583.
(7) Chuong, B.; Stevens, P. S. *J. Geophys. Res.* **2002**, *107*, 4612.
(8) Arnold, S. T.; Seeley, J. V.; Williamson, J. S.; Mundis, P. L.; Viggiano, A. A. *J. Phys. Chem. A* **2000**, *104*, 5511.
(9) Arnold, S. T.; Viggiano, A. A. *J. Phys. Chem. A* **2001**, *105*, 3527.
(10) Charlson, R. J.; Lovelock, J. E.; Andreae, M. O.; Warren, S. G. *Nature* **1987**, *326*, 655.
(11) Davis, D.; Chen, G.; Kasibhatla, P.; Jefferson, A.; Tanner, D.; Eisele, F.; Lenschow, D.; Neff, W.; Berresheim, H. *J. Geophys. Res.* **1998**, *103*, 1657.
(12) Nowak, J. B.; Davis, D. D.; Chen, G.; Eisele, F. L.; Mauldin, R. L.; Tanner, D. J.; Cantrell, C.; Kosciuch, E.; Bandy, A.; Thornton, D.; Clarke, A. *Geophys. Res. Lett.* **2001**, *28*, 2201.
(13) Barnes, I.; Becker, K. H.; Patroescu, I. *Geophys. Res. Lett.* **1994**, *21*, 2389.
(14) Barnes, I.; Becker, K. H.; Patroescu, I. *Atm. Environ.* **1996**, *30*, 1805.
(15) Sorensen, S.; Falbe-Hansen, H.; Mangoni, M.; Hjorth, J.; Jensen, N. R. *J. Atmos. Chem.* **1996**, *24*, 299.
(16) Arsene, C.; Barnes, I.; Becker, K. H. *Phys. Chem. Chem. Phys.* **1999**, *1*, 5463.
(17) Arsene, C.; Barnes, I.; Becker, K. H.; Mocanu, R. *Atm. Environ.* **2001**, *35*, 3769.
(18) Turnipseed, A. A.; Barone, S. B.; Ravishankara, A. R. *J. Phys. Chem.* **1996**, *100*, 14703.
(19) Barnes, I.; Bastian, V.; Becker, K. H.; Overath, R. *Int. J. Chem. Kinet.* **1991**, *23*, 579.
(20) Toumi, R. *Geophys. Res. Lett.* **1994**, *21*, 117.
(21) Bedjanian, Y.; Poulet, G.; Le Bras, G.; *Int. J. Chem. Kinet.* **1996**, *28*, 383.
(22) Ingham, T.; Bauer, D.; Sander, R.; Crutzen, P. J.; Crowley, J. N. *J. Phys. Chem. A* **1999**, *103*, 7199.
(23) Watts, S. F.; Brimblecomble, P.; Watson, A. *Atm. Environ.* **1990**, *24*, 353.
(24) Barnes, I.; Bastian, V.; Becker, K. H.; Martin, D. Fourier Transform IR studies of the reactions of dimethyl sulfoxide with OH, NO_3 and Cl radicals. *Biogenic Sulfur in the Environment*; 1989, Washington, DC.
(25) Hynes, A. J.; Wine, P. H. *J. Atmos. Chem.* **1996**, *24*, 23.
(26) Urbanski, S. P.; Stickel, R. E.; Wine, P. H. *J. Phys. Chem. A* **1998**, *102*, 10522.
(27) Falbe-Hansen, H.; Sorensen, S.; Jensen, N. R.; Pedersen, T.; Hjorth, J. *Atm. Environ.* **2000**, *34*, 1543.
(28) Arsene, C.; Barnes, I.; Becker, K. H.; Schneider, W. F.; Wallington, T. T.; Mihalopoulos, N.; Patroescu-Klotz, I. V. *Environ. Sci. Technol.* **2002**, *36*, 5155.
(29) Wang, L.; Zhang, J.; *Chem. Phys. Lett.* **2002**, *356*, 490.
(30) Christophorou, L. G.; Olthoff, J. K. *Int. J. Mass Spectrom.* **2001**, *205*, 27.
(31) Huey, L. G.; Hanson, D. R.; Howard, C. J. *J. Phys. Chem.* **1995**, *99*, 5001.
(32) Baldyga, J.; Pohorecki, R. *Chem. Eng. J.* **1995**, *58*, 183.
(33) Brodkey, R. S. *The phenomena of fluid motions*; Dover publications: New York, 1995.
(34) DeMore, W. B.; Sander, S. P.; Golden, D. M.; Hampson, R. F.; Kurylo, M. J.; Howard, C. J.; Ravishankara, A. R.; Colb, C. E.; Molina, M. J. *JPL Publication 97−4*, 1997.
(35) Williams, S.; Campos, M. F.; Midey, A. J.; Arnold, S. T.; Morris, R. A.; Viggiano, A. A. *J. Phys. Chem. A* **2002**, *106*, 997.
(36) Lovejoy, E. R.; Murrells, T. P.; Ravishankara, A. R.; Howard, C. J. *J. Phys. Chem.* **1990**, *94*, 2386.
(37) Distefano, G.; Foffani, A.; Innorta, G.; Pignataro, S. *Adv. Mass Spectrom.* **1971**, *5*, 696.
(38) Hynes, A. J.; Wine, P. H.; Semmes, D. H. *J. Phys. Chem.* **1986**, *90*, 4148.
(39) Yin, F.; Grosjean, D.; Seinfeld, J. *J. Atmos. Chem.* **1990**, *11*, 309.
(40) Kukui, A.; Bossoutrot, V.; Laverdet, G.; Le Bras, G. *J. Phys. Chem. A* **2000**, *104*, 935.
(41) Borissenko, B.; Kukui, A.; Laverdet, G.; Le Bras, G. *J. Phys. Chem. A* **2003**, *107*, 1155.
(42) Butkovskaya, N. I.; Setser, D. W. *Int. Rev. Phys. Chem.* **2002**, 1.
(43) Capaldo, K. P.; Pandis, S. N. *J. Geophys. Res.* **1997**, *102*, 23.251.
(44) Lucas, D. D.; Prinn, R. G. *J. Geophys. Res.* **2002**, *107*, 10.1029.
(45) Bardouki, H.; Barcellos da Rosa, M.; Mihalopoulos, N.; Palm, W.-U.; Zetzsch, C. *Atm. Environ.* **2002**, *36*, 4627.
(46) Pope, F. D.; Nicovich, J. M.; Wine, P. H. *Int. J. Chem. Kinet.* **2002**, *34*, 156.
(47) De Avillez Pereira, R.; Baulch, D. L.; Pilling, M. J.; Robertson, S. H.; Zeng, G. *J. Phys. Chem. A* **1997**, *101*, 9681.
(48) Yamada, F.; Slagle, I. R.; Gutman, D. *Chem. Phys. Lett.* **1981**, *83*, 409.
(49) Wollenhaupt, M.; Crowley, J. N. *J. Phys. Chem. A* **2000**, *104*, 6429.
(50) Baulch, D. L.; Cobos, C. J.; Cox, R. A.; Esser, C.; Frank, P.; Just, T.; Kerr, J. A.; Pilling, M. J.; Troe, J.; Walker, R. W.; Warnatz, J. *J. Phys. Chem. Ref. Data* **1992**, *21*, 411.
(51) D'Ottone, L.; Campuzano-Jost, P.; Bauer, D.; Hynes, A. J. *J. Phys. Chem. A* **2001**, *105*, 10538.
(52) Estupinan, E. G.; Nicovich, J. M.; Wine, P. H. *J. Phys. Chem. A* **2001**, *105*, 9697.
(53) Burkholder, J. B.; Ravishankara, A. R. *J. Phys. Chem. A* **2000**, *104*, 6752.